Rare Met.
https://doi.org/10.1007/s12598-024-02968-3

RARE METALS

ORIGINAL ARTICLE

Polymer-assisted in-situ growth of $Cs_3Sb_2Br_9$ on Co_3O_4 to boost sacrificial-agent-free photocatalytic CO_2 reduction

Ke Su, Su-Xian Yuan, You-Xiang Feng, Guang-Xing Dong, Yan-Fei Mu, Min Zhang*, Tong-Bu Lu*

Received: 28 April 2024 / Revised: 21 June 2024 / Accepted: 25 June 2024

Abstract Halide perovskite-based heterojunctions have emerged as promising candidates for solar energy conversion and storage due to their unique photophysical properties. However, the current bottleneck lies in the insufficient separation of photogenerated carriers at the interface, primarily due to challenges in the controllable growth of perovskite on the substrate. Herein, we present a growth strategy for depositing lead-free $Cs_3Sb_2Br_9$ perovskite nanocrystals onto the surface of Co_3O_4 with the assistance of polyacrylic acid (PAA), generating a step-scheme (S-scheme) heterojunction denoted as Co_3O_4–$Cs_3Sb_2Br_9$. The utilization of PAA as a template can effectively regulate the nucleation and growth of $Cs_3Sb_2Br_9$, thereby significantly enhancing the charge separation efficiency of the Co_3O_4–$Cs_3Sb_2Br_9$ heterojunction compared to its counterpart formed without PAA assistance. Under simulated solar light irradiation (100 $mW \cdot cm^{-2}$), the cerium-doped Co_3O_4–$Cs_3Sb_2Br_9$ heterojunction exhibits excellent photocatalytic CO_2 reduction activity without the need for any sacrificial agent. Specifically, the CO yield reaches up to 700.7 $\mu mol \cdot g^{-1} \cdot h^{-1}$, marking a 2.8-fold increase over the sample synthesized without PAA mediation. This polymer-assisted in-situ growth strategy should open up a new avenue for designing and developing more efficient photocatalytic materials based on halide perovskites.

Keywords Charge transfer; Heterojunction; In-situ growth; Lead-free perovskite; Photocatalytic CO_2 reduction

1 Introduction

Natural photosynthesis is an amazing process that can convert CO_2 and water into energy-rich organic matter while releasing oxygen solely by harnessing abundant solar energy. This process not only sustains human activities but also plays a pivotal role in maintaining the energy flow and carbon–oxygen balance in nature over extended periods [1, 2]. However, the rapid population and economic growth of the past century have led to extensive fossil fuel consumption, resulting in escalating CO_2 emissions and triggering the climate crisis, which constrains sustainable human development. In this context, artificial photosynthesis technology, drawing inspiration from natural photosynthesis, has garnered increasing attention over the past decade [3–10], which can convert CO_2 and water into chemicals and oxygen by capturing sunlight through a photocatalyst. Apart from robust sunlight responsiveness, photocatalysts must possess potent redox capabilities to drive both the half-reactions of CO_2 reduction and H_2O oxidation, thus ensuring efficient artificial photosynthesis [11–14].

Supplementary Information The online version contains supplementary material available at https://doi.org/10.1007/s12598-024-02968-3.

K. Su, S.-X. Yuan, Y.-X. Feng, G.-X. Dong, M. Zhang*, T.-B. Lu*
MOE International Joint Laboratory of Materials Microstructure, Institute for New Energy Materials and Low Carbon Technologies, School of Materials Science and Engineering, Tianjin University of Technology, Tianjin 300384, China
e-mail: zm2016@email.tjut.edu.cn

T.-B. Lu
e-mail: lutongbu@tjut.edu.cn

Y.-F. Mu
School of Chemistry and Chemical Engineering, Yangzhou University, Jiangsu 225009, China

Published online: 17 February 2025

In recent years, lead-free metal halide perovskites have emerged as promising photocatalytic candidates among various developed photocatalysts due to their cost-effectiveness, eco-friendliness, superb light responsiveness and adjustable band structures [15–18]. Notably, antimony-based perovskites exhibit commendable stability and a relatively prolonged carrier lifetime, with band structures capable of concurrently driving CO_2 reduction and H_2O oxidation [19]. Nevertheless, their sluggish water oxidation capability poses a significant challenge to enhancing the photocatalytic activity of CO_2 reduction. Current research primarily focuses on combining perovskites with other semiconductors through electrostatic attraction or in-situ growth to create step-scheme (S-scheme) heterojunctions, aiming to augment the photocatalytic activity of CO_2 reduction [20, 21]. Yet, S-scheme heterojunctions produced by existing methods still have some deficiencies. For instance, electrostatic attraction may result in inadequate contact between the two components, impeding charge transfer. Additionally, the in-situ growth of antimony-based perovskites on semiconductor surfaces may exacerbate non-radiative recombination due to the rapid crystallization kinetics and low formation energy of perovskites, making them prone to aggregation and crystalline defect [22]. This undermines efforts to enhance the photocatalytic activity of CO_2 reduction. As a result, the controlled synthesis of antimony-based perovskite nanocrystals on semiconductor substrates for constructing S-scheme heterojunctions remains a challenge.

Herein, we employed porous hollow Co_3O_4 as a substrate and elaborately introduced the polymer polyacrylic acid (PAA) onto its surface to precisely control the nucleation and growth processes of $Cs_3Sb_2Br_9$ perovskite nanocrystals, ultimately achieving in-situ construction of a Co_3O_4–$Cs_3Sb_2Br_9$ S-scheme heterojunction. The strategy is primarily based on the following important considerations: (1) Co_3O_4, a black crystalline oxide semiconductor, is a common candidate for photocatalytic water oxidation due to its deep valence band edge, high stability and wide visible response [23, 24]. (2) Co_3O_4 is also a typical p-type semiconductor, which exhibits a significant work function difference from the n-type semiconductor $Cs_3Sb_2Br_9$. This enables the generation of a strong built-in electric field and a large degree of band bending at the contact interface of the Co_3O_4–$Cs_3Sb_2Br_9$ heterojunction, beneficial for the formation of an S-scheme charge transfer pathway and the rapid separation and transfer of photogenerated carriers [25, 26]. (3) The introduction of PAA serves a dual purpose: firstly, it forms intermediate complexes with the $Cs_3Sb_2Br_9$ precursor, redirecting random nucleation towards thermodynamically favorable growth; secondly, PAA confines the space for perovskite nanocrystal growth, effectively preventing extensive aggregation and significantly enhancing the active surface area for photocatalytic reactions. As anticipated, the prepared Co_3O_4–$Cs_3Sb_2Br_9$ composite exhibits a significant enhancement in photocatalytic performance. The cerium-doped Co_3O_4–$Cs_3Sb_2Br_9$ photocatalyst achieves an impressive CO_2 reduction to CO yield of up to 700.7 $\mu mol \cdot g^{-1} \cdot h^{-1}$ without the addition of any organic sacrificial agents. This not only far surpasses the performance of the individual components but also notably outperforms the counterpart synthesized without PAA assistance.

2 Experimental

The materials, instrumentation and characterization details are elaborated in the Supplementary Information. Zeolitic Imidazolate Frameworks-67 (ZIF-67), Co_3O_4 and $Cs_3Sb_2Br_9$ were synthesized following previously reported methods with some modifications [27, 28] (further details provided in the Supplementary Information).

Preparation of Co_3O_4-PAA composite: Initially, chloroacetic acid (CA) was anchored onto the surface of porous Co_3O_4 nanocrystals, serving as an initiator for PAA polymerization. Specifically, a mixture consisting of Co_3O_4 (50 mg) and CA (95 mg) was dispersed in deionized water (10 mL) and magnetically stirred (200 rpm) at 60 °C in an Ar atmosphere for 24 h. The resulting product, designated as Co_3O_4-CA, underwent three washes with deionized water to eliminate excess CA and was then redispersed in deionized water (5 mL) for further utilization. Subsequently, PAA brushes were grafted onto the surface of Co_3O_4 nanocages via activators regenerated by electron transfer atom transfer radical polymerization (ARGET-ATRP). The $CuCl_2$/1,1,4,7,7-pentamethyl diethylenetriamine (PMDETA) complex, comprised of $CuCl_2$ (13.4 mg) and PMDETA (208 μL) dissolved in N, N-dimethylformamide (DMF, 5 mL), catalyzed the ARGET-ATRP reaction. Sequential addition of L-ascorbic acid sodium (AAS, 30 mg), $CuCl_2$/PMDETA (500 μL) and Co_3O_4-CA dispersion (5 mL) were performed in an Ar atmosphere. Then, sodium acrylate (NaAA, 100 mg) dissolved in ethanol was introduced into the system, and the reaction proceeded for 12 h at 80 °C. The resulting Co_3O_4-PAA composite was washed three times with ethanol and deionized water before being freeze-dried for further application.

Preparation of Co_3O_4–$Cs_3Sb_2Br_9$ composite: Initially, Co_3O_4-PAA (10 mg) was mixed with DMF (6.5 mL) for 24 h at room temperature to ensure uniform dispersion. Subsequently, CsBr (44.7 mg) was added and stirred for an additional 12 h until complete dissolution. Then $SbBr_3$ (50.6 mg) was introduced to the solution containing Co_3O_4-PAA and CsBr and stirred for another 24 h.

Following this, a solution of DMF (1 mL) containing Co_3O_4-PAA and $Cs_3Sb_2Br_9$ precursors was swiftly injected into preheated toluene (10 mL) at 50 °C, with vigorous stirring, to promptly form Co_3O_4–$Cs_3Sb_2Br_9$ composites. Finally, the Co_3O_4–$Cs_3Sb_2Br_9$ composite was washed three times with isopropanol (IPA) and vacuum-dried at 60 °C. The molar ratio between Co_3O_4 and $Cs_3Sb_2Br_9$ is 1:10. By adjusting the quantity of CsBr (19.1 and 83.0 mg) while maintaining a molar ratio of CsBr:$SbBr_3$ = 3:2, other compositions labeled as Co_3O_4–$Cs_3Sb_2Br_9$-5 and Co_3O_4–$Cs_3Sb_2Br_9$-20 were obtained.

Preparation of Ce/Co_3O_4–$Cs_3Sb_2Br_9$ composite: Initially, Ce-doped ZIF-67 was synthesized following the same procedure as pure ZIF-67, but with the addition of $Ce(NO_3)_3 \cdot 6H_2O$ (1%, relative to the molar amount of $Co(NO_3)_2 \cdot 6H_2O$) to the methanol solution of $Co(NO_3)_2 \cdot 6H_2O$. Subsequently, Ce-doped ZIF-67 served as the precursor for synthesizing Ce-doped Co_3O_4, Ce-doped Co_3O_4-PAA and Ce-doped Co_3O_4–$Cs_3Sb_2Br_9$ in sequence. The resulting composite was designated as Ce/Co_3O_4–$Cs_3Sb_2Br_9$. The concentration of doped Ce can be adjusted by varying the amount of $Ce(NO_3)_3 \cdot 6H_2O$ (0.5% and 2% relative to the molar amount of $Co(NO_3)_2 \cdot 6H_2O$) added to the methanol solution.

Preparation of Co_3O_4:$Cs_3Sb_2Br_9$ composite: The synthesis of Co_3O_4:$Cs_3Sb_2Br_9$ followed the same process as Co_3O_4–$Cs_3Sb_2Br_9$, except that pure Co_3O_4 was utilized in the reaction system instead of Co_3O_4-PAA.

3 Results and discussion

3.1 Preparation and characterization of Co_3O_4–$Cs_3Sb_2Br_9$ composite

The synthesis process of the Co_3O_4–$Cs_3Sb_2Br_9$ composite is schematically represented in Fig. 1a. Initially, the metal–organic framework material, ZIF-67, is constructed and serves as a precursor. This precursor undergoes a two-step calcination process, yielding porous Co_3O_4. Following this, chloroacetic acids are grafted onto the surface of Co_3O_4 where carbonyl groups coordinate with the cobalt atoms. The subsequent in-situ growth of brush-like PAA on the surface of Co_3O_4, via the ARGET-ATRP reaction [29], leads to the formation of the Co_3O_4-PAA composite. This treatment notably enhances the dispersion of Co_3O_4 particles in water, due to the hydrophilic property of PAA (Fig. S1), thus affirming successful grafting of PAA onto the Co_3O_4 surface. Next, the $Cs_3Sb_2Br_9$ precursor is selectively introduced into the spaces occupied by the PAA chains. This loading is achieved through prolonged stirring at room temperature [30]. The process capitalizes on the strong coordination interactions between the carboxylic acid groups in the PAA chains and the metal atoms present in the lead-free perovskite $Cs_3Sb_2Br_9$ precursor. After this, the Co_3O_4-PAA dispersion, now containing the $Cs_3Sb_2Br_9$ precursor, is rapidly injected into toluene maintained at 50 °C. Owing to the low solubility of $Cs_3Sb_2Br_9$ in toluene, $Cs_3Sb_2Br_9$ nanocrystals swiftly nucleate and grow within the confines of the PAA chains. This ultimately results in the creation of a composite where $Cs_3Sb_2Br_9$ nanocrystals have grown in-situ on the Co_3O_4 surface, denoted as Co_3O_4–$Cs_3Sb_2Br_9$.

The morphology and composition of Co_3O_4–$Cs_3Sb_2Br_9$ were initially investigated through scanning electron microscopy (SEM) measurements. Figure 1b clearly illustrates that the as-prepared Co_3O_4 particles exhibit a distinct hollow structure while retaining the rhombic dodecahedral morphology from the parent ZIF-67 (Fig. S2). Furthermore, a high-resolution SEM (HRSEM) image reveals that these dodecahedral Co_3O_4 structures are made up of numerous interconnected Co_3O_4 nanoparticles (Fig. 1c). This unique porous and hollow structure of Co_3O_4 endows a substantial specific surface area providing ample space for the growth of $Cs_3Sb_2Br_9$ and numerous active sites for photocatalytic reactions. The average size of Co_3O_4 particles is approximately 300 nm (Fig. S3). It is worth noting that the size of Co_3O_4 remains largely unchanged after the growth of PAA (Fig. S4), maintaining its characteristic hollow rhombic dodecahedron shape. The SEM image presented in Fig. 1d showcases the composite after PAA-mediated growth of $Cs_3Sb_2Br_9$ on the Co_3O_4 surface. In contrast to the smooth edges of Co_3O_4, the surface of Co_3O_4–$Cs_3Sb_2Br_9$ is visibly adorned with protruding particles. HRSEM image further highlights the growth and infiltration of these nanoparticles on the surface and within the pores of Co_3O_4 (Fig. 1e). To further investigate the elemental distribution of Co_3O_4–$Cs_3Sb_2Br_9$, energy dispersive X-ray spectroscopy (EDS) mapping measurements were conducted. As demonstrated in Fig. 1f–k, the elements of Cs, Sb, Br, Co and O are evenly distributed within the composite material, affirming the tight in-situ growth of $Cs_3Sb_2Br_9$ on the Co_3O_4 surface. The PAA chains coating the Co_3O_4 surface effectively adsorb $Cs_3Sb_2Br_9$ precursors, enabling $Cs_3Sb_2Br_9$ to crystallize on the Co_3O_4 surface, thus ensuring close contact between them. Additionally, since $Cs_3Sb_2Br_9$ forms in-situ within the domain-limited space provided by PAA, the formation of large-sized $Cs_3Sb_2Br_9$ is prevented. In comparison, the morphology of Co_3O_4–$Cs_3Sb_2Br_9$ composite differs significantly from its Co_3O_4:$Cs_3Sb_2Br_9$ counterpart (where $Cs_3Sb_2Br_9$ grows directly on the Co_3O_4 surface without PAA). In the latter case, $Cs_3Sb_2Br_9$ freely grows on Co_3O_4, resulting in bulk materials of uneven size due to the absence of constraints imposed by PAA (Fig. S5).

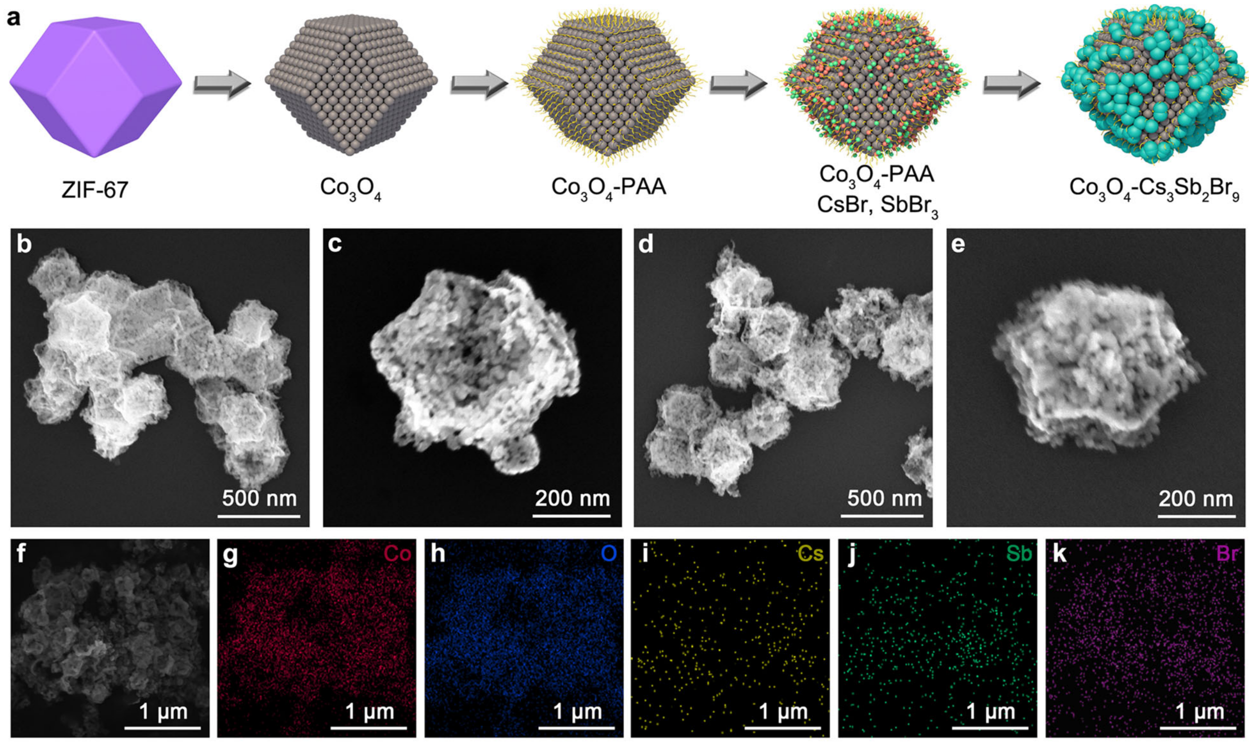

Fig. 1 **a** Schematic illustration of formation process of Co_3O_4–$Cs_3Sb_2Br_9$ heterojunction; **b** SEM and **c** HRSEM images of Co_3O_4; **d** SEM and **e** HRSEM images of Co_3O_4–$Cs_3Sb_2Br_9$; **f** SEM image of Co_3O_4–$Cs_3Sb_2Br_9$ and corresponding elemental mapping images for **g** Co, **h** O, **i** Cs, **j** Sb, and **k** Br

Powder X-ray diffraction (PXRD) measurements were conducted to delve deeper into the crystal structure of the samples. As presented in Fig. S6, XRD pattern of ZIF-67 concurs with the simulated results. The diffraction peaks of the as-prepared Co_3O_4 are situated at 19.0°, 31.3°, 36.9°, 44.8°, 59.3° and 65.3°, corresponding to the (111), (220), (311), (400), (511) and (440) planes of the cubic phase Co_3O_4 (JCPDS No. 76-1802), respectively. Notably, no diffraction peaks associated with ZIF-67 are discernible in the XRD pattern of Co_3O_4, suggesting complete conversion of ZIF-67 to Co_3O_4 after calcination at temperatures exceeding 400 °C for 2 h. XRD diffraction signals of Co_3O_4 after grafting PAA are consistent with those of the initial Co_3O_4, indicating the absence of Co_3O_4 decomposition during PAA formation. Additionally, the Raman spectrum of Co_3O_4-PAA aligns with that of Co_3O_4 (Fig. S7), where distinct E_g, F_{2g} and A_{1g} signals are observable before and after PAA grafting, located at 477.2, 515.8 and 680.6 cm^{-1}, respectively [31, 32]. This further validates that the growth of PAA did not compromise the Co_3O_4 structure.

The presence of PAA within the Co_3O_4-PAA composite was subsequently determined through Fourier transform infrared spectroscopy (FTIR), X-ray photoelectron spectroscopy (XPS) and thermogravimetric analysis (TG) characterizations. As illustrated in Fig. S8, alongside the peaks at 660 and 570 cm^{-1} attributed to Co−O, Co_3O_4-PAA manifests additional vibrational peaks corresponding to bending vibration of hydroxyl (−OH) groups at approximately 3381 cm^{-1} and stretching vibration of carbonyl (C=O) groups at around 1631 cm^{-1}, indicative of the grafting of PAA brushes [28, 29]. Furthermore, Fig. S9 demonstrates that the XPS spectrum of Co_3O_4-PAA can be deconvoluted into four peaks: Co−O, O−H, C−O and C=O. The signals of O−H, C−O and C=O signals can be attributed to the abundant carboxyl groups present in PAA [33]. In contrast, pure Co_3O_4 exhibits no C=O signal, and the O−H and C−O signals are relatively weak, possibly due to adsorbed H_2O and impurity carbon on the Co_3O_4 surface. Additionally, TG analysis reveals a weight loss of approximately 30% for Co_3O_4-PAA between 200 and 450 °C (Fig. S10), further confirming the successful grafting of PAA.

Figure 2a displays the XRD diffraction pattern of $Cs_3Sb_2Br_9$, showing peaks at 22.5°, 27.6°, 31.9°, 39.4°, 45.9° and 54.4°, which correspond to the (110), (201), (022), (300), (220) and (223) planes of the hexagonal phase standard pattern of $Cs_3Sb_2Br_9$ (JCPDS No. 77-1055). In the Co_3O_4–$Cs_3Sb_2Br_9$ composite, characteristic diffraction peaks indicating high crystallinity of $Cs_3Sb_2Br_9$ are distinctly visible. Additionally, a characteristic diffraction peak at 36.9° corresponding to the (311) plane of Co_3O_4 is

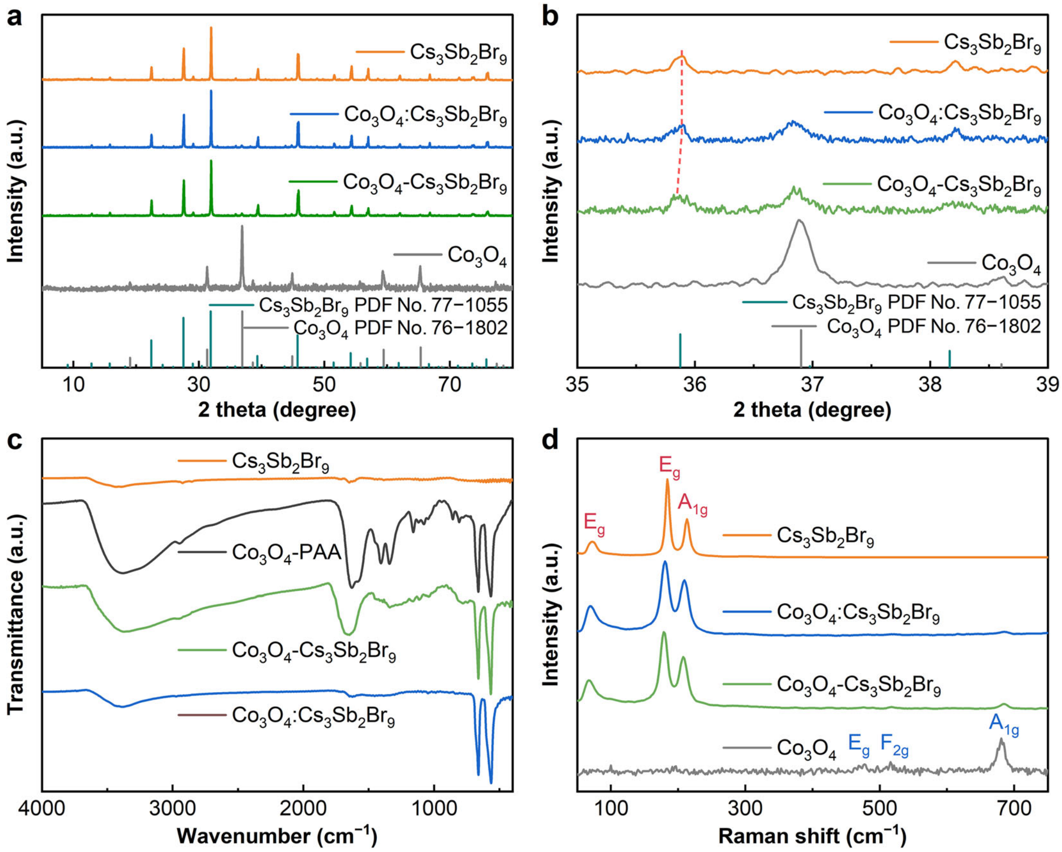

Fig. 2 **a** PXRD patterns and **b** their enlarged views of $Cs_3Sb_2Br_9$, Co_3O_4:$Cs_3Sb_2Br_9$, Co_3O_4–$Cs_3Sb_2Br_9$ and Co_3O_4; **c** FTIR spectra of $Cs_3Sb_2Br_9$, Co_3O_4-PAA, Co_3O_4–$Cs_3Sb_2Br_9$ and Co_3O_4:$Cs_3Sb_2Br_9$; **d** Raman spectra of $Cs_3Sb_2Br_9$, Co_3O_4:$Cs_3Sb_2Br_9$, Co_3O_4–$Cs_3Sb_2Br_9$ and Co_3O_4

observable in the enlarged XRD pattern in Fig. 2b. These results signify the successful synthesis of the Co_3O_4–$Cs_3Sb_2Br_9$ composite while maintaining the crystal structures. Analogous observations are noted for the Co_3O_4:$Cs_3Sb_2Br_9$ composite. Figure 2c illustrates the Fourier transform infrared spectra of Co_3O_4 and Co_3O_4–$Cs_3Sb_2Br_9$, revealing distinct characteristic peaks at 660 and 570 cm^{-1}, possibly attributed to the characteristic vibration mode of Co−O. Moreover, vibration peaks of −OH and C=O belonging to PAA are evident in Co_3O_4–$Cs_3Sb_2Br_9$ but are less discernible in Co_3O_4:$Cs_3Sb_2Br_9$. Pure $Cs_3Sb_2Br_9$ does not exhibit unique characteristic infrared signals due to its ionic crystal nature. In Fig. 2d, the Raman characteristic peaks of $Cs_3Sb_2Br_9$ can be observed at 72.4, 183.9 and 213.0 cm^{-1}, attributed to the strong E_g and A_{1g} modes of the hexagonal phase of $Cs_3Sb_2Br_9$ [34]. In the Raman spectrum of Co_3O_4–$Cs_3Sb_2Br_9$, a noticeable blue shift of the E_g and A_{1g} modes is apparent, suggesting that the introduction of Co_3O_4 and PAA restricts the growth of $Cs_3Sb_2Br_9$. This leads to the formation of defects such as vacancies, resulting in lattice expansion and mode softening [35]. This observation is corroborated by the slight low-angle shift of the diffraction peak belonging to $Cs_3Sb_2Br_9$ (located at 35.9°) in Fig. 2b. For Co_3O_4:$Cs_3Sb_2Br_9$, this shift is less pronounced. Additionally, the characteristic peak at 680 cm^{-1} observed in both Co_3O_4–$Cs_3Sb_2Br_9$ and Co_3O_4:$Cs_3Sb_2Br_9$, is attributed to the A_{1g} mode of Co_3O_4.

3.2 Interfacial charge transfer dynamics of Co_3O_4–$Cs_3Sb_2Br_9$ heterojunction

Given the crucial role of heterojunction energy band alignment in determining interfacial charge transfer orientation, ultraviolet–visible diffuse reflectance spectroscopy (UV–Vis DRS) and ultraviolet photoelectron spectroscopy (UPS) measurements were conducted to ascertain the thermodynamic properties of Co_3O_4 and $Cs_3Sb_2Br_9$. As depicted in Fig. 3a, individual Co_3O_4 demonstrates a relatively broad absorption in the visible light region, with an absorption edge at approximately 850 nm. However, its absorption coefficient is limited. In contrast, $Cs_3Sb_2Br_9$ exhibits excellent light absorption capacity in the ultraviolet–visible light region below ∼

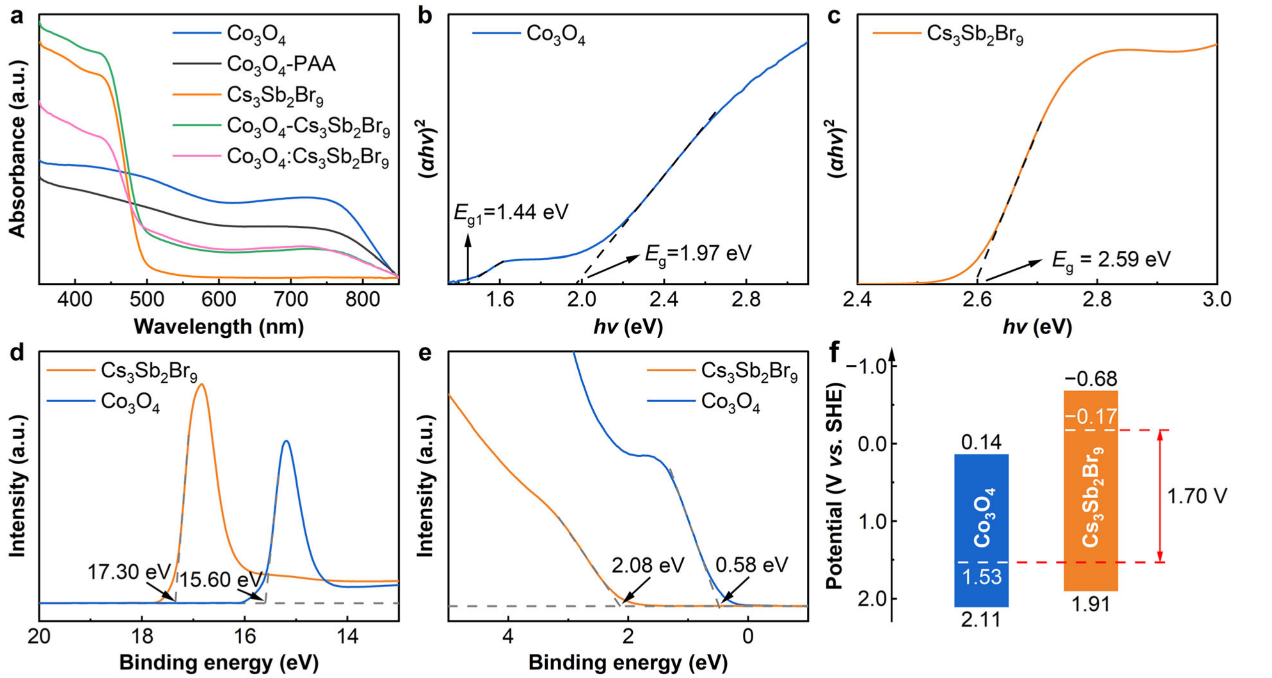

Fig. 3 **a** UV−Vis DRS spectra of Co_3O_4, Co_3O_4-PAA, $Cs_3Sb_2Br_9$, Co_3O_4–$Cs_3Sb_2Br_9$ and Co_3O_4:$Cs_3Sb_2Br_9$; Tauc plots of **b** Co_3O_4 and **c** $Cs_3Sb_2Br_9$; UPS spectra of Co_3O_4 and $Cs_3Sb_2Br_9$ in **d** cutoff and **e** onset energy regions; **f** energy band diagrams of Co_3O_4 and $Cs_3Sb_2Br_9$ before contact

500 nm. Notably, the distinct absorption characteristics of both Co_3O_4 and $Cs_3Sb_2Br_9$ are clearly discernible in the Co_3O_4–$Cs_3Sb_2Br_9$ composite, further confirming successful composite material synthesis. The converted Tauc plot for Co_3O_4, shown in Fig. 3b, displays two intersections with the abscissa, with E_{g1} representing the O^{2-}-Co^{3+} excitation [36]. As a result, the optical bandgap (E_g) of the Co_3O_4 is determined to be 1.97 eV. Similarly, Fig. 3c reveals that the E_g of the $Cs_3Sb_2Br_9$ is 2.59 eV. UPS spectra of Co_3O_4 and $Cs_3Sb_2Br_9$, presented in Fig. 3d, e, facilitate the calculation of valence band edge potentials (E_{VB}) of Co_3O_4 and $Cs_3Sb_2Br_9$, which are 2.11 and 1.91 V, respectively, relative to the standard hydrogen electrode (SHE, $E_{SHE} = -4.09 - E_{vacuum}$). By combining the values of E_g and E_{VB}, the conduction band potentials (E_{CB}) of Co_3O_4 and $Cs_3Sb_2Br_9$ are deduced to be 0.14 and −0.68 V vs. SHE, respectively. Furthermore, the flat-band potentials (Fig. S11) of Co_3O_4 and $Cs_3Sb_2Br_9$, determined from Mott-Schottky curve measurements, are 2.11 and −0.68 V vs. SHE, respectively, which aligns with the UPS measurements. Notably, staggered energy band alignments are clearly visible in the Co_3O_4–$Cs_3Sb_2Br_9$ composite, as illustrated in Fig. 3f.

The interaction and free electron migration between Co_3O_4 and $Cs_3Sb_2Br_9$ upon their contact were investigated using high-resolution XPS measurements. As shown in Fig. 4a−c, the binding energies of Cs 3d, Sb 3d and Br 3d in the Co_3O_4–$Cs_3Sb_2Br_9$ composite exhibit a perceptible shift toward higher energies, ranging from 0.11 to 0.16 eV compared to pure $Cs_3Sb_2Br_9$. Conversely, when compared to pure Co_3O_4, the binding energy of Co 2p in Co_3O_4–$Cs_3Sb_2Br_9$ shifts toward lower energies, decreasing by approximately 0.30 to 0.57 eV (Fig. 4d). These shifts in elemental binding energies suggest that during the formation of the heterojunction, the electron density decreases on $Cs_3Sb_2Br_9$ and increases on Co_3O_4. This finding implies that upon the formation of the heterojunction, electrons migrate from $Cs_3Sb_2Br_9$ to Co_3O_4 across the interface, which aligns with previous research [37]. Although Co_3O_4:$Cs_3Sb_2Br_9$ exhibits a similar trend of charge transfer as Co_3O_4–$Cs_3Sb_2Br_9$, the magnitude of binding energy shifts observed for individual elements is relatively smaller (Fig. 4e, f). This difference suggests that in the Co_3O_4–$Cs_3Sb_2Br_9$ heterojunction, the confined space provided by the PAA allows $Cs_3Sb_2Br_9$ to densely populate the surface and pores of Co_3O_4, enabling strong electron coupling and facilitating rapid charge transfer at the interface.

The interfacial charge transfer and separation efficiency of the samples were further characterized through transient photocurrent response and electrochemical impedance spectroscopy (EIS) measurements. As demonstrated in Fig. S12, the Co_3O_4–$Cs_3Sb_2Br_9$ composite exhibits significantly enhanced photocurrent density, surpassing that of Co_3O_4, $Cs_3Sb_2Br_9$ and Co_3O_4:$Cs_3Sb_2Br_9$ by approximately 10.9, 3.7 and 1.7 times, respectively. Additionally, Co_3O_4–$Cs_3Sb_2Br_9$ demonstrates the smallest electrochemical

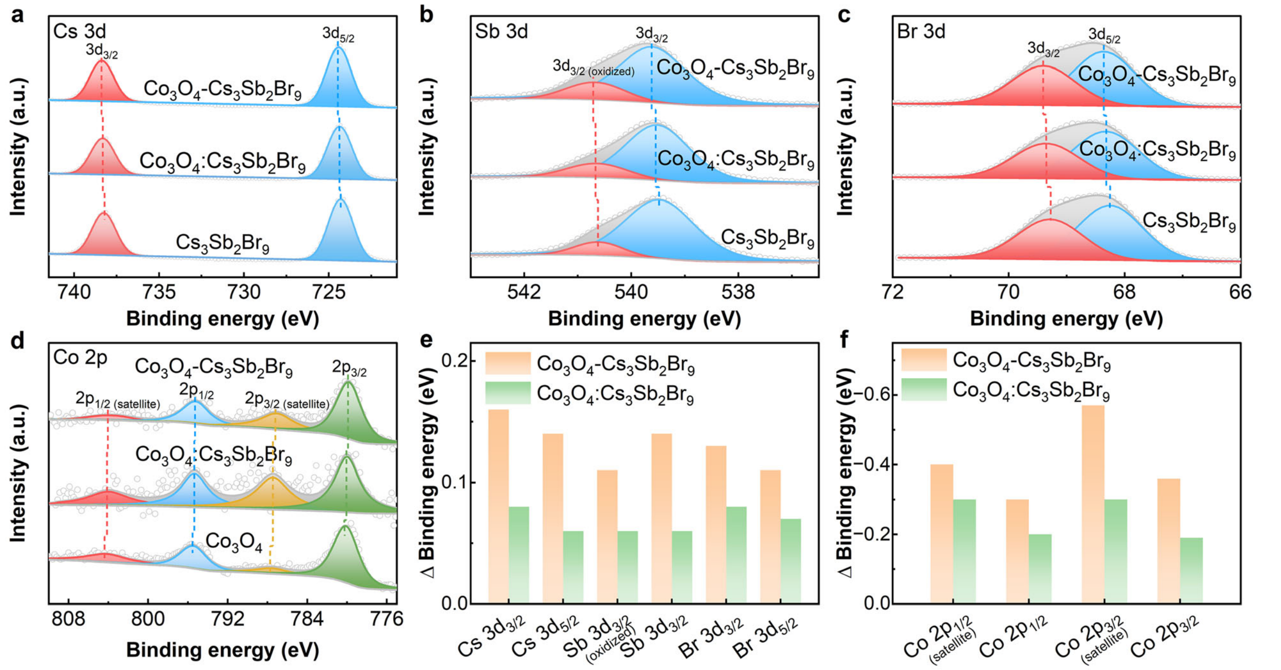

Fig. 4 High-resolution XPS spectra of **a** Cs 3d, **b** Sb 3d and **c** Br 3d in $Cs_3Sb_2Br_9$, Co_3O_4:$Cs_3Sb_2Br_9$ and Co_3O_4–$Cs_3Sb_2Br_9$; **d** high-resolution XPS spectra of Co 2p in Co_3O_4, Co_3O_4:$Cs_3Sb_2Br_9$ and Co_3O_4–$Cs_3Sb_2Br_9$; binding energy shift in Co_3O_4–$Cs_3Sb_2Br_9$ and Co_3O_4:$Cs_3Sb_2Br_9$ relating to **e** $Cs_3Sb_2Br_9$ and **f** Co_3O_4, respectively

impedance diameter under illumination, indicating excellent interfacial charge transport properties (Fig. S13 and Table S1). This can be attributed to the tight and controlled growth of $Cs_3Sb_2Br_9$ on the Co_3O_4 surface, reducing the recombination rate of the photogenerated electron–hole pairs and accelerating the photogenerated carrier migration process. Furthermore, transient photoluminescence measurements were conducted to elucidate the dynamics of photogenerated carriers. As illustrated in Fig. S14, the decay curves were precisely analyzed and found to align perfectly with the biexponential fitting model, with the corresponding fitting parameters listed in Table S2. The results reveal that the photoluminescence lifetime of Co_3O_4–$Cs_3Sb_2Br_9$ (1.52 ns) is perceivably shorter than that of the pristine $Cs_3Sb_2Br_9$ nanocrystals (1.82 ns) and Co_3O_4:$Cs_3Sb_2Br_9$ (1.75 ns), indicating a higher photogenerated carrier separation efficiency of Co_3O_4–$Cs_3Sb_2Br_9$.

3.3 Photocatalytic CO_2 reduction activity

In a gas–solid reaction equipment, H_2O vapor served as the reducing agent to evaluate the activity of several photocatalysts in CO_2 photoreduction. A Xe lamp simulator with a light intensity of 100 $mW \cdot cm^{-2}$ was employed to simulate visible light conditions. To underscore the advantages of the PAA-mediated heterojunction in photocatalytic reactions, a comparative study was conducted among pure Co_3O_4, $Cs_3Sb_2Br_9$, Co_3O_4:$Cs_3Sb_2Br_9$ and Co_3O_4–$Cs_3Sb_2Br_9$ composites for photocatalytic CO_2 reduction under identical conditions. Gas chromatography analysis revealed CO as the primary gaseous product, with no other significant reduction products across all the samples (Fig. S15). Despite the E_{CB} value of $Cs_3Sb_2Br_9$ being more negative than the reduction potential required for CO_2-to-CH_4 conversion (0.17 V vs. SHE), no appreciable CH_4 was detected. This may be attributed to the complexity of the CO_2-to-CH_4 conversion, which necessitates an eight-electron transfer process. Here, the hydrogenation of the key intermediate CO competes with its desorption. Figure 5a provides a comprehensive visualization of the CO generation rates of various photocatalysts. The photocatalytic CO_2 reduction using Co_3O_4 yields unsatisfactory results, with a CO rate of 25.2 $\mu mol \cdot g^{-1} \cdot h^{-1}$. This should be attributed to its limited thermodynamic driving force for reduction reaction and its inadequate carrier separation capability. Similarly, pure $Cs_3Sb_2Br_9$, despite its ideal energy band structure, also exhibits a low CO yield of 46.6 $\mu mol \cdot g^{-1} \cdot h^{-1}$, primarily because of its poor water oxidizing capacity.

In stark contrast, the PAA-mediated Co_3O_4–$Cs_3Sb_2Br_9$ heterojunction, distinguished by its unique energy band configuration and effective charge separation and transfer, demonstrates remarkable performance in photoreduction CO_2. With the optimized composite ratio (where the actual mass and molar ratios of Co_3O_4 to $Cs_3Sb_2Br_9$ are 1:0.71 and 1:0.13, respectively, Table S3), the average CO yield

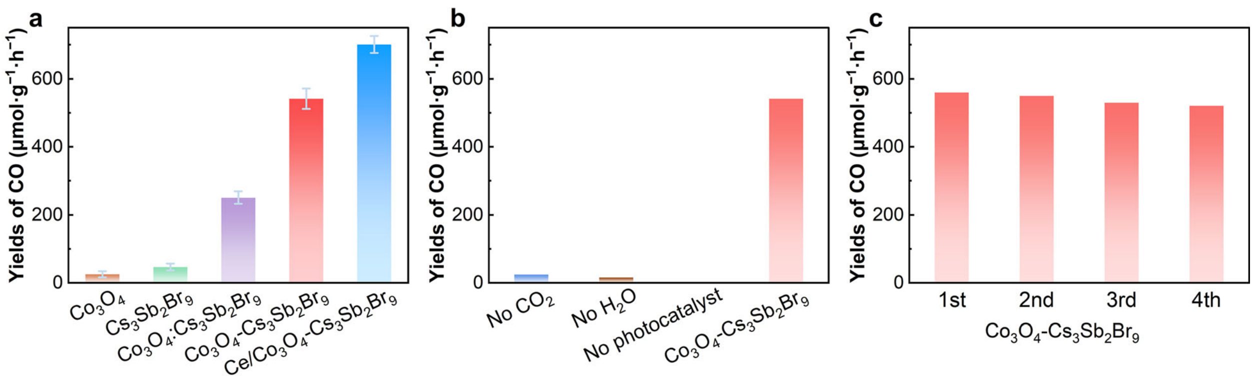

Fig. 5 **a** Yields of CO under irradiation for 4 h with Co_3O_4, $Cs_3Sb_2Br_9$, Co_3O_4:$Cs_3Sb_2Br_9$, Co_3O_4–$Cs_3Sb_2Br_9$ and Ce/Co_3O_4–$Cs_3Sb_2Br_9$ as photocatalysts at a light intensity of 100 mW·cm^{-2}; **b** CO_2 reduction performance under various conditions; **c** yields of CO for 4 cycles with 1 h each using Co_3O_4–$Cs_3Sb_2Br_9$ as photocatalyst

of Co_3O_4–$Cs_3Sb_2Br_9$ soars to 541.9 μmol·g^{-1}·h^{-1}. This is significantly higher than that the yields of Co_3O_4 and $Cs_3Sb_2Br_9$, by 21.5 and 11.6 times, respectively. It is worth mentioning that the composite, where $Cs_3Sb_2Br_9$ was directly grown on the Co_3O_4 surface (Co_3O_4:$Cs_3Sb_2Br_9$), exhibits a comparatively lower CO production rate of 251.0 μmol·g^{-1}·h^{-1}. This disparity can be traced back to the absence of the confining effect provided by PAA, leading to the growth of larger $Cs_3Sb_2Br_9$ particles on the Co_3O_4 surface, resulting in increased photogenerated carrier recombination within these larger particles. Additionally, the limited contact area between Co_3O_4 and $Cs_3Sb_2Br_9$ may have hindered effective carrier separation. Given that the slow water oxidation kinetics is the rate-limiting factor in the photocatalytic CO_2 reduction process, doping active metal ions into Co_3O_4 can further enhance catalytic efficiency by improving charge separation efficiency and increasing catalytic activity [38]. A cerium-doped Co_3O_4–$Cs_3Sb_2Br_9$ composite was also synthesized, designated as Ce/Co_3O_4–$Cs_3Sb_2Br_9$. This composite achieves an impressive average CO generation rate of 700.7 μmol·g^{-1}·h^{-1}, which is 27.8, 15.0 and 2.8 times higher than that of Co_3O_4, $Cs_3Sb_2Br_9$ and Co_3O_4:$Cs_3Sb_2Br_9$ composite, respectively (Figs. 4a, S16, S17). This performance significantly surpasses other reported halide perovskite-based photocatalysts under similar conditions (Table S4). Meanwhile, the oxidation product O_2 of Co_3O_4–$Cs_3Sb_2Br_9$ and Ce/Co_3O_4–$Cs_3Sb_2Br_9$ was quantified, averaging 281.2 and 359.6 μmol·g^{-1}·h^{-1}, respectively, maintaining a nearly stoichiometric of 1:2 ratio with respect to the yield of CO (Fig. S18).

Using Co_3O_4–$Cs_3Sb_2Br_9$ as the photocatalyst, a series of control experiments were further conducted to pinpoint the sources of CO and O_2. As shown in Fig. 5b, only a minimal amount of CO was detected in the absence of CO_2 or water vapor. This indicates that CO originated from the photoreduction of CO_2, and electrons solely originated from H_2O oxidation. These deductions were further corroborated by isotope-labeled experiments employing $^{13}CO_2$ and $H_2{}^{18}O$. Mass spectrometry analysis of the products (Fig. S19) revealed m/z = 29 corresponding to ^{13}CO and m/z = 36 belonging to $^{18}O_2$, confirming that the CO and O_2 products originated from CO_2 photoreduction and water oxidation, respectively. Moreover, the stability of the photocatalyst was estimated through cycling experiments. As shown in Fig. 5c, the percentage decrease in CO production rates after four cycles was less than 10%, indicating the good stability of Co_3O_4–$Cs_3Sb_2Br_9$ in the gas–solid reaction system. Furthermore, XRD analysis conducted before and after photocatalysis confirmed that the structure of Co_3O_4–$Cs_3Sb_2Br_9$ remained well-preserved after the photocatalytic reaction (Fig. S20).

3.4 S-scheme mode and photocatalytic mechanism

The carrier migration mode within the Co_3O_4–$Cs_3Sb_2Br_9$ heterojunction was further investigated and analyzed. Mott-Schottky measurements unveiled negative and positive slope curves for Co_3O_4 and $Cs_3Sb_2Br_9$, respectively, at varying frequencies. These curves indicate p-type and n-type semiconductor behaviors for Co_3O_4 and $Cs_3Sb_2Br_9$, respectively (Fig. S11). Consequently, their Fermi level (E_F) positions are biased towards the corresponding valence band and conduction band edges, as determined by UPS measurements (Fig. 3d, e). These measurements yielded E_F values of 1.53 and −0.17 eV vs. SHE for Co_3O_4 and $Cs_3Sb_2Br_9$, respectively (Fig. S21a). The notably higher E_F of $Cs_3Sb_2Br_9$ relative to Co_3O_4 prompts the migration of free electrons from $Cs_3Sb_2Br_9$ to Co_3O_4 upon contact, establishing E_F equilibrium within the space charge region of Co_3O_4–$Cs_3Sb_2Br_9$ heterojunction. This observation is consistent with XPS results obtained in the dark state (Fig. 4), creating an interfacial built-in electric field directing from $Cs_3Sb_2Br_9$ to Co_3O_4. Concurrently, the band edges of $Cs_3Sb_2Br_9$ bend upward due to electron loss, while the band edges of Co_3O_4 bend downward due to electron accumulation (Fig. S21b) [39–42].

Under light irradiation, electrons in both Co_3O_4 and $Cs_3Sb_2Br_9$ are excited, transitioning from the valence band maximum (VB) to the conduction band minimum (CB). The built-in electric field, coupled with band edge bending, facilitates the recombination of excited electrons (e^-) from Co_3O_4 with holes (h^+) from $Cs_3Sb_2Br_9$. This process prevents the transfer of photogenerated electrons from $Cs_3Sb_2Br_9$ to Co_3O_4 (Fig. S21c). This suggests an interfacial charge transfer mechanism akin to the S-scheme operating within the Co_3O_4–$Cs_3Sb_2Br_9$ heterojunction. This

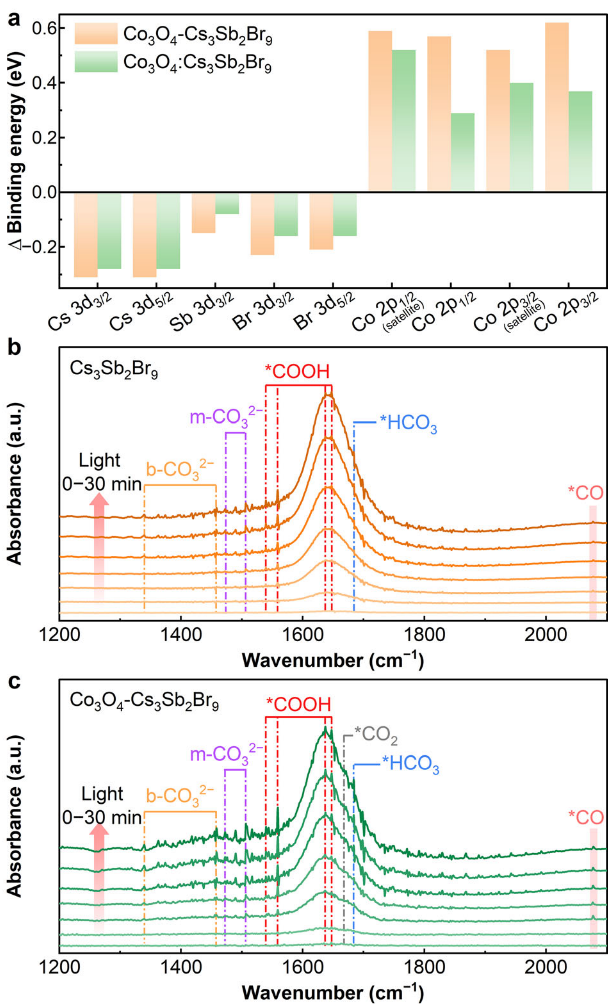

Fig. 6 **a** Light-induced binding energy shift (Δ binding energy) in Co_3O_4–$Cs_3Sb_2Br_9$ and Co_3O_4:$Cs_3Sb_2Br_9$, as derived from in-situ photo-excited XPS measurements; in-situ FTIR spectra for photocatalytic CO_2 reduction over **b** $Cs_3Sb_2Br_9$ and **c** Co_3O_4–$Cs_3Sb_2Br_9$

mechanism is further supported by in-situ photo-excited XPS measurements (Figs. S22, S23). The photoinduced variation values of elemental binding energies for Co_3O_4-$Cs_3Sb_2Br_9$ and Co_3O_4:$Cs_3Sb_2Br_9$ are summarized in Fig. 6a. Notably, light irradiation leads to an increase in the binding energy of the associated elements of Co_3O_4, while the binding energy of the associated element of $Cs_3Sb_2Br_9$ decreases. This signifies the respective consumption of photogenerated electrons in Co_3O_4 and holes in $Cs_3Sb_2Br_9$. Although this S-scheme charge transfer mechanism consumes some e^- and h^+, it preserves the electrons in the conduction band of $Cs_3Sb_2Br_9$ and the holes in the valence band of Co_3O_4. These retained charge carriers possess stronger reduction and oxidation capabilities.

In addition, the adsorption and activation mechanisms during the CO_2 reduction process were analyzed by conducting in-situ FTIR measurements. Based on the thermodynamic and kinetic properties of photogenerated carriers in the Co_3O_4–$Cs_3Sb_2Br_9$ composite, it is speculated that the photoreduction process of CO_2 is primarily facilitated by the $Cs_3Sb_2Br_9$ component. To validate this hypothesis, in-situ FTIR spectral data were collected for both $Cs_3Sb_2Br_9$ and Co_3O_4–$Cs_3Sb_2Br_9$, as detailed in Fig. 6b, c. Prior to conducting the light experiment, argon gas was utilized to purge any air from the test system and eliminate other potential interfering factors, thereby ensuring accurate experimental results. No characteristic signals of the intermediates were detected during this purging process. However, upon exposure to light and the continuous introduction of moist CO_2 into the test system, characteristic signals of intermediates gradually emerged. With increasing exposure to light, both $Cs_3Sb_2Br_9$ and Co_3O_4–$Cs_3Sb_2Br_9$ exhibited similar signal peaks in the spectral region of 1200–2100 cm^{-1}. This suggests that within the Co_3O_4–$Cs_3Sb_2Br_9$ heterojunction, $Cs_3Sb_2Br_9$ serves as the active component for CO_2 reduction. Specifically, the signal peaks located at 1339 and 1458 cm^{-1} correspond to the characteristic vibrational mode of bidentate carbonate (b-CO_3^{2-}) [43, 44]. Peaks at 1472 and 1507 cm^{-1} are attributed to the characteristic vibration of monodentate carbonate (m-CO_3^{2-}) [43, 45]. The peak at 1684 cm^{-1} represents the vibrational mode of *HCO_3 [46]. A unique set of signal peaks was observed at 1539, 1558, 1637, and 1647 cm^{-1}, indicating the characteristic vibrations of *COOH [47]. This intermediate plays a crucial role in the conversion of CO_2 to CO, and its emergence is linked to the adsorption of *CO (with signals located at 2077 cm^{-1}) on the catalyst surface [48]. Comparatively, for Co_3O_4–$Cs_3Sb_2Br_9$, the peak at 1667 cm^{-1} belongs to the *CO_2 group, as depicted in Fig. 6c. The intensity of this peak increases with the prolonged illumination, suggesting that the introduction of Co_3O_4 aids in charge separation and significantly boosts CO_2 reduction activity [35, 48]. Drawing from the aforementioned experimental findings, we deduced the reaction pathway of photocatalytic CO_2 reduction on the Co_3O_4–$Cs_3Sb_2Br_9$ composite. Upon photon absorption by the Co_3O_4–$Cs_3Sb_2Br_9$, photogenerated electrons and holes are rapidly generated and separated. Notably, electrons primarily accumulate in the $Cs_3Sb_2Br_9$ component, and the holes predominantly concentrate in the Co_3O_4 component. Following this, CO_2 molecules undergo adsorbed, activated and a proton-coupled electron transfer process. This sequence leads to the formation of the $(Cs_3Sb_2Br_9)\cdots COOH$ intermediate and the cleavage of the C–OH bond, ultimately resulting in the reduction to CO. Simultaneously, holes and protons oxidize H_2O to O_2 on the Co_3O_4 surface, supplying electrons for CO_2 reduction [49].

4 Conclusion

In summary, a lead-free halide perovskite-based S-scheme heterojunction of Co_3O_4-$Cs_3Sb_2Br_9$ was successfully constructed via PAA-assisted in-situ growth of $Cs_3Sb_2Br_9$ on Co_3O_4. This heterojunction demonstrates remarkable performance in CO_2 photoreduction, achieving a CO yield of 700.7 $\mu mol \cdot g^{-1} \cdot h^{-1}$ using water as an electron source. Microstructure characterization revealed that the employment of PAA facilitates controlled nucleation and growth of $Cs_3Sb_2Br_9$ by adsorbing its precursor within a confined space. This approach inhibits the formation of large-sized $Cs_3Sb_2Br_9$ crystals, fostering close contact between Co_3O_4 and $Cs_3Sb_2Br_9$. This close contact is conducive to photogenerated carrier separation via an S-scheme pathway, as evidenced by electrochemical, photophysical and in-situ photoexcited XPS measurements. This work provides an effective strategy for the controlled growth of halide perovskite nanocrystals on a semiconductor substrate, ensuring a tight interface. This breakthrough paves a new avenue for enhancing energy conversion performance with halide perovskite-based photocatalysts.

Acknowledgements This work was financially supported by the National Key R&D Program of China (No. 2022YFA1502902), the National Natural Science Foundation of China (Nos. U21A20286 and 22475152), the Natural Science Foundation of Tianjin City (No. 17JCJQJC43800), the Programme of Introducing Talents of Discipline to Universities (111 Project) and Tianjin Research Innovation Project for Postgraduate Students (No. 2022BKY156).

Declarations

Conflict of interests The authors declare that they have no conflict of interest.

References

[1] Wang Y, Godin R, Durrant JR, Tang JW. Efficient hole trapping in carbon dot/oxygen-modified carbon nitride heterojunction photocatalysts for enhanced methanol production from CO_2 under neutral conditions. Angew Chem Int Ed. 2021;60(38):20811. https://doi.org/10.1002/anie.202105570.

[2] Guo Q, Liang F, Li XB, Gao YJ, Huang MY, Wang Y, Xia SG, Gao XY, Gan QC, Lin ZS, Tung CH, Wu LZ. Efficient and selective CO_2 reduction integrated with organic synthesis by solar energy. Chem. 2019;5(10):2605. https://doi.org/10.1016/j.chempr.2019.06.019.

[3] Wang T, Gong JL. Sacrificing nothing to reduce CO_2. Nat Energy. 2020;5(9):642. https://doi.org/10.1038/s41560-020-00688-3.

[4] Ye S, Ding CM, Liu MY, Wang AQ, Huang QG, Li C. Water oxidation catalysts for artificial photosynthesis. Adv Mater. 2019;31(50):1902069. https://doi.org/10.1002/adma.201902069.

[5] Navarro-Jaén S, Virginie M, Bonin J, Robert M, Wojcieszak R, Khodakov AY. Highlights and challenges in the selective reduction of carbon dioxide to methanol. Nat Rev Chem. 2021;5(8):564. https://doi.org/10.1038/s41570-021-00289-y.

[6] Loh JYY, Kherani NP, Ozin GA. Persistent CO_2 photocatalysis for solar fuels in the dark. Nat Sustain. 2021;4(6):466. https://doi.org/10.1038/s41893-021-00681-y.

[7] Huang HN, Shi R, Li ZH, Zhao JQ, Su CL, Zhang TR. Triphase photocatalytic CO_2 reduction over silver-decorated titanium oxide at a gas–water boundary. Angew Chem Int Ed. 2022;61(17): e202200802. https://doi.org/10.1002/anie.202200802.

[8] Zhou P, Luo MC, Guo SJ. Optimizing the semiconductor–metal-single-atom interaction for photocatalytic reactivity. Nat Rev Chem. 2022;6(11):823. https://doi.org/10.1038/s41570-022-00434-1.

[9] Sun LJ, Su HW, Liu QQ, Hu J, Wang LL, Tang H. A review on photocatalytic systems capable of synchronously utilizing photogenerated electrons and holes. Rare Met. 2022;41(7):2387. https://doi.org/10.1007/s12598-022-01966-7.

[10] Zhou AQ, Yang JM, Zhu XW, Zhu XL, Liu JY, Zhong K, Chen HX, Chu JY, Du YS, Song YH, Qian JC, Li HM, Xu H. Self-assembly construction of NiCo LDH/ultrathin g-C_3N_4 nanosheets photocatalyst for enhanced CO_2 reduction and charge separation mechanism study. Rare Met. 2022;41(6):2118. https://doi.org/10.1007/s12598-022-01960-z.

[11] Zhang WH, Mohamed AR, Ong WJ. Z-scheme photocatalytic systems for carbon dioxide reduction: Where are we now? Angew Chem Int Ed. 2020;59(51):22894. https://doi.org/10.1002/anie.201914925.

[12] Wang LX, Zhu BC, Zhang JJ, Ghasemi JB, Mousavi M, Yu JG. S-scheme heterojunction photocatalysts for CO_2 reduction. Matter. 2022;5(12):4187. https://doi.org/10.1016/j.matt.2022.09.009.

[13] Zeng RJ, Liu TY, Qiu MH, Tan H, Gu Y, Ye N, Dong ZQ, Li L, Lin FX, Sun Q, Zhang QH, Gu L, Luo MC, Tang DP, Guo SJ. High-volumetric density atomic cobalt on multishell $Zn_xCd_{1-x}S$ boosts photocatalytic CO_2 reduction. J Am Chem Soc. 2024;146(14):9721. https://doi.org/10.1021/jacs.3c13827.

[14] Jiang Z, Xu XH, Ma YH, Cho HS, Ding D, Wang C, Wu J, Oleynikov P, Jia M, Cheng J, Zhou Y, Terasaki O, Peng TY, Zan L, Deng HX. Filling metal-organic framework mesopores with TiO_2 for CO_2 photoreduction. Nature. 2020;586(7830):549. https://doi.org/10.1038/s41586-020-2738-2.

[15] Supriya S. Recent trends and morphology mechanisms of rare-earth based $BiFeO_3$ nano perovskites with excellent photocatalytic performances. J Rare Earths. 2023;41(3):331. https://doi.org/10.1016/j.jre.2022.08.011.

[16] Zhang ZZ, Yang YY, Wang YY, Yang LL, Li Q, Chen LX, Xu DS. Revealing the A-site effect of lead-free $A_3Sb_2Br_9$ perovskite in photocatalytic C(sp^3)−H bond activation. Angew Chem Int Ed. 2020;59(41):18136. https://doi.org/10.1002/anie.202005495.
[17] Lu C, Itanze DS, Aragon AG, Ma X, Li H, Ucer KB, Hewitt C, Carroll DL, Williams RT, Qiu YJ, Geyer SM. Correction: synthesis of lead-free $Cs_3Sb_2Br_9$ perovskite alternative nanocrystals with enhanced photocatalytic CO_2 reduction activity. Nanoscale. 2022;14(22):8200. https://doi.org/10.1039/D2NR90107B.
[18] Wu JH, Zhao W, Chen M, Liu CX, Chen JC, Chen Z. Recent advance in visible-light-driven photocatalysis on lead-free halide perovskites. Chin J Rare Met. 2022;46(1):96. https://doi.org/10.13373/j.cnki.cjrm.XY21040007.
[19] Liu YL, Yang CL, Wang MS, Ma XG, Yi YG. Theoretical insight into the optoelectronic properties of lead-free perovskite derivatives of $Cs_3Sb_2X_9$ (X = Cl, Br, I). J Mater Sci. 2019;54(6):4732. https://doi.org/10.1007/s10853-018-3162-y.
[20] Xu FY, Meng K, Cheng B, Wang SY, Xu JS, Yu JG. Unique S-scheme heterojunctions in self-assembled $TiO_2/CsPbBr_3$ hybrids for CO_2 photoreduction. Nat Commun. 2020;11(1):4613. https://doi.org/10.1038/s41467-020-18350-7.
[21] Zhang ZJ, Wang XS, Li DB, Chu YQ, Xu JY. Regulating oxygen vacancies and fermi level of mesoporous CeO_{2-x} for intensified built-in electric field and boosted charge separation of $Cs_3Bi_2Br_9/CeO_{2-x}$ S-scheme heterojunction. Small. 2024;20(2):2305566. https://doi.org/10.1002/smll.202305566.
[22] Bi DQ, Yi CY, Luo JS, Décoppet JD, Zhang F, Zakeeruddin SM, Li X, Hagfeldt A, Grätzel M. Polymer-templated nucleation and crystal growth of perovskite films for solar cells with efficiency greater than 21%. Nat Energy. 2016;1(10):16142. https://doi.org/10.1038/nenergy.2016.142.
[23] Subagyo R, Yudhowijoyo A, Sholeha NA, Hutagalung SS, Prasetyoko D, Birowosuto MD, Arramel A, Jiang JZ, Kusumawati Y. Recent advances of modification effect in Co_3O_4-based catalyst towards highly efficient photocatalysis. J Colloid Interface Sci. 2023;650:1550. https://doi.org/10.1016/j.jcis.2023.07.117.
[24] Kang WC, Wei RF, Yin H, Li DF, Chen Z, Huang QG, Zhang PF, Jing HW, Wang XL, Li C. Unraveling sequential oxidation kinetics and determining roles of multi-cobalt active sites on Co_3O_4 catalyst for water oxidation. J Am Chem Soc. 2023;145(6):3470. https://doi.org/10.1021/jacs.2c11508.
[25] Hao MM, Wei DQ, Li ZH. Rational design of an efficient S--scheme heterojunction of CdS/Bi_2WO_6-S nanocomposites for photocatalytic CO_2 reduction. Energy Fuels. 2022;36(19):11524. https://doi.org/10.1021/acs.energyfuels.2c01076.
[26] Su B, Zheng M, Lin W, Lu XF, Luan DY, Wang SB, Lou XW. S-scheme $Co_9S_8@Cd_{0.8}Zn_{0.2}S$-DETA hierarchical nanocages bearing organic CO_2 activators for photocatalytic syngas production. Adv Energy Mater. 2023;13(15):2203290. https://doi.org/10.1002/aenm.202203290.
[27] Pan Y, Sun KA, Liu SJ, Cao X, Wu KL, Cheong WC, Chen Z, Wang Y, Li Y, Liu YQ, Wang DS, Peng Q, Chen C, Li YD. Core–shell ZIF-8@ZIF-67-derived CoP nanoparticle-embedded N-doped carbon nanotube hollow polyhedron for efficient overall water splitting. J Am Chem Soc. 2018;140(7):2610. https://doi.org/10.1021/jacs.7b12420.
[28] Chen YM, Yu L, Lou XW. Hierarchical tubular structures composed of Co_3O_4 hollow nanoparticles and carbon nanotubes for lithium storage. Angew Chem Int Ed. 2016;55(20):5990. https://doi.org/10.1002/anie.201600133.
[29] Xie LQ, Jin WW, Zuo XR, Ji SL, Nan WB, Chen HL, Gao ST, Zhang QQ. Construction of small-sized superparamagnetic Janus nanoparticles and their application in cancer combined chemotherapy and magnetic hyperthermia. Biomater Sci. 2020;8(5):1431. https://doi.org/10.1039/C9BM01880H.
[30] Liang S, Zhang MY, He S, Tian MK, Choi W, Lian TQ, Lin ZQ. Metal halide perovskite nanorods with tailored dimensions, compositions and stabilities. Nat Synth. 2023;2(8):719. https://doi.org/10.1038/s44160-023-00307-5.
[31] Jin X, Duan Y, Liu DP, Feng XL, Li W, Zhang Z, Zhang Y. CO oxidation catalyzed by two-dimensional Co_3O_4/CeO_2 nanosheets. ACS Appl Nano Mater. 2019;2(9):5769. https://doi.org/10.1021/acsanm.9b01225.
[32] Wang L, Wan JW, Zhao YS, Yang NL, Wang D. Hollow multi-shelled structures of Co_3O_4 dodecahedron with unique crystal orientation for enhanced photocatalytic CO_2 reduction. J Am Chem Soc. 2019;141(6):2238. https://doi.org/10.1021/jacs.8b13528.
[33] Qi DF, Xu J, Zhou YT, Zhang H, Shi JQ, He K, Yuan YF, Luo J, Wang S, Wang Y. Cyclodextrin-supported $Co(OH)_2$ clusters as electrocatalysts for efficient and selective H_2O_2 synthesis. Angew Chem Int Ed. 2023;62(37):e202307355. https://doi.org/10.1002/anie.202307355.
[34] Liu P, Liu Y, Zhang SW, Li JZ, Wang CY, Zhao C, Nie PB, Dong YH, Zhang X, Zhao SX, Wei GD. Lead-free $Cs_3Sb_2Br_9$ single crystals for high performance narrowband photodetector. Adv Opt Mater. 2020;8(21):2001072. https://doi.org/10.1002/adom.202001072.
[35] Xu QJ, Jiang JW, Wang XF, Duan LY, Guo H. Understanding oxygen vacant hollow structure $CeO_2@In_2O_3$ heterojunction to promote CO_2 reduction. Rare Met. 2023;42(6):1888. https://doi.org/10.1007/s12598-022-02244-2.
[36] Makhlouf SA, Bakr ZH, Aly KI, Moustafa MS. Structural, electrical and optical properties of Co_3O_4 nanoparticles. Superlattices Microstruct. 2013;64:107. https://doi.org/10.1016/j.spmi.2013.09.023.
[37] Su K, Yuan SX, Wu LY, Liu ZL, Zhang M, Lu TB. Nanoscale Janus Z-scheme heterojunction for boosting artificial photosynthesis. Small. 2023;19(32):2301192. https://doi.org/10.1002/smll.202301192.
[38] Shan JQ, Ye C, Chen SM, Sun TL, Jiao Y, Liu LM, Zhu CZ, Song L, Han Y, Jaroniec M, Zhu YH, Zheng Y, Qiao SZ. Short-range ordered iridium single atoms integrated into cobalt oxide spinel structure for highly efficient electrocatalytic water oxidation. J Am Chem Soc. 2021;143(13):5201. https://doi.org/10.1021/jacs.1c01525.
[39] Huang ZF, Song JJ, Wang X, Pan L, Li K, Zhang XW, Wang L, Zou JJ. Switching charge transfer of $C_3N_4/W_{18}O_{49}$ from type-II to Z-scheme by interfacial band bending for highly efficient photocatalytic hydrogen evolution. Nano Energy. 2017;40:308. https://doi.org/10.1016/j.nanoen.2017.08.032.
[40] Wang XH, Wang XH, Huang JF, Li SX, Meng A, Li ZJ. Interfacial chemical bond and internal electric field modulated Z-scheme S_v-$ZnIn_2S_4/MoSe_2$ photocatalyst for efficient hydrogen evolution. Nat Commun. 2021;12(1):4112. https://doi.org/10.1038/s41467-021-24511-z.
[41] Chen GJ, Zhou ZR, Li BF, Lin XH, Yang C, Fang YX, Lin W, Hou YD, Zhang GG, Wang SB. S-scheme heterojunction of crystalline carbon nitride nanosheets and ultrafine WO_3 nanoparticles for photocatalytic CO_2 reduction. J Environ Sci. 2024;140:103. https://doi.org/10.1016/j.jes.2023.05.028.
[42] Su B, Huang HW, Ding ZX, Roeffaers MBJ, Wang SB, Long JL. S-scheme $CoTiO_3/Cd_{9.51}Zn_{0.49}S_{10}$ heterostructures for visible-light driven photocatalytic CO_2 reduction. J Mater Sci Technol. 2022;124:164. https://doi.org/10.1016/j.jmst.2022.01.030.
[43] Liu LJ, Jiang YQ, Zhao HL, Chen JT, Cheng JL, Yang KS, Li Y. Engineering coexposed {001} and {101} facets in oxygen-deficient TiO_2 nanocrystals for enhanced CO_2 photoreduction under visible light. ACS Catal. 2016;6(2):1097. https://doi.org/10.1021/acscatal.5b02098.

[44] Zhou GL, Yang JM, Zhu XW, Li QD, Yu Q, El-alami W, Wang CT, She YB, Qian JC, Xu H, Li HM. Cryo-induced closely bonded heterostructure for effective CO_2 conversion: the case of ultrathin BP nanosheets/g-C_3N_4. J Energy Chem. 2020;49:89. https://doi.org/10.1016/j.jechem.2020.01.020.
[45] Mo QL, Li JL, Xu SR, Wang K, Ge XZ, Xiao Y, Wu G, Xiao FX. Unexpected insulating polymer maneuvered solar CO_2-to-syngas conversion. Adv Func Mater. 2023;33(7):2210332. https://doi.org/10.1002/adfm.202210332.
[46] Barman S, Singh A, Rahimi FA, Maji TK. Metal-free catalysis: a redox-active donor–acceptor conjugated microporous polymer for selective visible-light-driven CO_2 reduction to CH_4. J Am Chem Soc. 2021;143(39):16284. https://doi.org/10.1021/jacs.1c07916.
[47] Li XD, Li L, Chen GB, Chu XY, Liu XH, Naisa C, Pohl D, Löffler M, Feng XL. Accessing parity-forbidden d-d transitions for photocatalytic CO_2 reduction driven by infrared light. Nat Commun. 2023;14(1):4034. https://doi.org/10.1038/s41467-023-39666-0.
[48] Li J, Huang HL, Xue WJ, Sun K, Song XH, Wu CR, Nie L, Li Y, Liu CY, Pan Y, Jiang HL, Mei DH, Zhong CL. Self-adaptive dual-metal-site pairs in metal-organic frameworks for selective CO_2 photoreduction to CH_4. Nat Catal. 2021;4(8):719. https://doi.org/10.1038/s41929-021-00665-3.
[49] Feng YX, Su K, Liu ZL, Yuan SX, Mu YF, Zhang M, Lu TB. A halide perovskite based ternary heterojunction with multi-shell hollow structure for stable and efficient artificial photosynthesis. Appl Catal B Environ Energy. 2024;347:123821. https://doi.org/10.1016/j.apcatb.2024.123821.